IN VIVO *39*: 1394-1413 (2025)
doi: 10.21873/invivo.13942

Gefitinib Facilitates Bone Fracture Healing *via* Inhibition of the EGFR Pathway and Counteracting SOX9-driven Bone Metabolic Reprogramming

NING XU[1,2*], GONGWU YUAN[3,4*], WENBO ZENG[5], XIMING LIU[6], MA WAN[1,2], SUYANG XU[1,2], YIKANG BI[1,2], HAI HU[1,2], YAFENG XU[1,2] and SHENGHUI LAN[1,2]

[1]Department of Orthopedics, The Eighth People's Hospital, Jiangsu University, Shanghai, P.R. China;
[2]Department of Orthopedics, Xuhui Branch of The Sixth People's Hospital, Shanghai Jiao Tong University, Shanghai, P.R. China;
[3]Department of Orthopedics, Hubei Provincial Hospital of Integrated Chinese & Western Medicine, Wuhan, P.R. China;
[4]College of Acupuncture and Orthopedics, Hubei University of Chinese Medicine, Wuhan, P.R. China;
[5]Department of Orthopedics, The First Affiliated Hospital of Chongqing Medical University, Chongqing, P.R. China;
[6]Department of Orthopedics, General Hospital of Central Theater Command, Wuhan, P.R. China

Abstract

Background/Aim: To investigate the role of epidermal growth factor receptor (EGFR) inhibition in enhancing bone fracture healing by modulating box transcription factor 9 (SOX9) and bone metabolism.

Materials and Methods: A rat femoral fracture model was used. Techniques included histological analysis, X-ray scoring, micro-computed tomography, immunohistochemistry, and biomechanical testing. Serum markers were analyzed with enzyme-linked immunosorbent assay, while quantitative real-time polymerase chain reaction and western blotting assessed molecular pathways. Metabolic changes were measured using a Seahorse analyzer. An EGFR inhibitor, gefitinib, was used to examine its impact on periosteal stem cell differentiation and metabolism.

Results: EGFR inhibition improved bone callus formation and quality, increased cartilage callus, and upregulated bone formation markers. Gefitinib enhanced oxidative phosphorylation and fatty acid oxidation, counteracting negative effects from lipid-reduced serum on osteoblastic differentiation of periosteal stem cell. SOX9 overexpression reduced the benefits of EGFR inhibition.

Conclusion: Gefitinib enhances bone fracture healing by modulating lipid metabolism through SOX9, suggesting its potential as a therapeutic agent for improving fracture outcomes.

*These Authors contributed equally to this study.

Yafeng Xu, Department of Orthopedics, The Eighth People's Hospital, Jiangsu University, 8 Caobao Road, Xuhui District, Shanghai 200235, P.R. China. E-mail: qyzsxyf521@alumni.sjtu.edu.cn and Shenghui Lan, Department of Orthopedics, The Eighth People's Hospital, Jiangsu University, 8 Caobao Road, Xuhui District, Shanghai 200235, P.R. China. E-mail: d200978245@alumni.hust.edu.cn

Received November 5, 2024 | Revised February 19, 2025 | Accepted March 4, 2025

Keywords: Bone metabolism, epidermal growth factor receptor, EGFR, fracture healing, gefitinib, SRY-box transcription factor 9, SOX9.

Introduction

Bone fracture healing is a multifaceted physiological process that involves intricate regulation of various intracellular and extracellular signaling pathways across different stages of healing (1). There has been a discernible decline in recent years in the mortality rate among patients with multiple traumas. However, there has been a concurrent rise in the incidence of poor fracture healing outcomes, such as delayed healing (2). Hence, there is an urgent need for studies elucidating the molecular mechanisms underlying fracture healing, aiming to advance treatment strategies for patients afflicted with this condition.

Numerous studies have corroborated the significant role of the epidermal growth factor receptor (EGFR) in bone metabolism, encompassing processes such as bone formation and resorption. Specifically, a recent study by Dong *et al.* identified a critical role of epiregulin in regulating osteoblast differentiation through EGFR-mediated inactivation of the mechanistic target of rapamycin kinase complex 1 pathway (3). Relaxin-2 stimulates osteogenic differentiation through activating EGF/EGFR signaling (4). A study by Wang *et al.* confirmed that macrophage-derived amphiregulin promoted the osteogenic differentiation of chondrocytes through EGFR/YAP axis and transforming growth factor-beta activation (5). Shen *et al.* reported SOX2 as a positive regulatory factor during osteoclast differentiation partly through the EGFR and extracellular-regulated kinase signaling pathways (6). Additionally, Jia *et al.* indicated that blocking the EGFR pathway reduced M1 macrophage polarization and osteoclast differentiation, alleviating titanium particle-induced bone resorption (7). Although the potential influence of EGFR on osteoclast growth is recognized, its specific role in fracture healing remains poorly understood.

Gefitinib, an EGFR tyrosine kinase inhibitor, is widely used in the treatment of non-small-cell lung cancer. By inhibiting EGFR signal transduction, gefitinib suppresses cancer cell proliferation and survival, demonstrating significant clinical efficacy (8). Furthermore, gefitinib treatment promoted senescence of osteoprogenitors and accelerated cortical bone degeneration in middle-aged mice by reducing EGFR signaling (9).

SRY-Box transcription factor 9 (SOX9) is a critical transcription factor extensively involved in chondrogenesis and the regulation of bone development (10). SOX9-driven gene expression changes are central to bone metabolic reprogramming (11) and significantly impact the fracture healing process (12, 13). Furthermore, abnormal bone metabolism during bone repair may delaying the healing process (14). Therefore, modulating SOX9 activity might be a crucial strategy for enhancing fracture healing.

This study explored the role of gefitinib in fracture healing, hypothesizing that it promotes this process by inhibiting the EGFR signaling pathway and interacting with SOX9-mediated bone metabolic reprogramming. Through *in vivo* and *in vitro* experiments, the study aimed to clarify the effects of gefitinib on bone cell function and fracture repair, potentially positioning gefitinib as a therapeutic agent for bone fracture treatment and offering new strategies for improving patient recovery.

Materials and Methods

Ethics statement. This study was approved by the Committee of Experimental Animals of the Eighth People's Hospital, Jiangsu University (Shanghai, PR China; approval no. ECM202310165). All procedures related to animal testing were conducted in accordance with the Guidance for the Care and Use of Laboratory Animals issued by the Ministry of Science and Technology Department of the People's Republic of China.

Animals and surgical procedures. A total of 104 4-week-old male Sprague-Dawley rats (*Rattus norvegicus*; Experimental Animal Research Center of Hubei Province, PR China) were adaptively fed for 1 week and were subsequently anesthetized by intraperitoneal injection of chloral hydrate (300 mg/kg). An intramedullary 1.0-mm-diameter Kirschner wire was retrogradely inserted into the greater trochanter *via* piercing from the femoral intercondylar, and the wire was then cut at the level of the articular surface of the knee and at the margin of the greater trochanter. An incision was made at the right lateral thigh, and the right femur was exposed by separating the *vastus lateralis*; subsequently, a mid-femoral transverse osteotomy was carried out with a bone scissors.

After surgery under anesthesia, X-ray examination was carried out on the right femur of all rats to observe the degree of displacement and the type of fractures, which were transverse or short oblique to the middle part of the femur. The model rats were split at random into a gefitinib-treated experimental group (n=52) and a vehicle-treated control group (n=52). Rats in the gefitinib-treated group were administered gefitinib (100 ml/kg) dissolved in 0.5% methyl cellulose through oral gavage daily for 6 weeks, while rats in the vehicle-treated control group were treated with 0.5% methyl cellulose. X-Ray examination was carried out on the right femur on days 0, 7, 14, 21, 28, and 42.

Following the completion of experimental procedures, the rats were euthanized using CO_2 inhalation. The CO_2 flow rate was set to displace 20% of the chamber volume per minute, ensuring a gradual and humane euthanasia process. This was followed by cervical dislocation to confirm death before cardiac puncture was performed to collect blood samples to measure serum osteogenic markers and osteoclastic markers. The volume of blood collected from each rat was approximately 8-10 ml. The weight of the rats at the time of sacrifice was recorded, with the average weight being 220-330 g. Femurs were harvested for histological analysis and micro-computed tomography (MCT); callus within 3 mm of the proximal and distal fracture line was collected for assay by quantitative real-time polymerase chain reaction (qRT-PCR).

The criteria for humane endpoints included: Loss of 15% or more body weight; severe lameness or inability to reach food or water; signs of severe pain or distress unrelieved by analgesics; non-healing or infected wounds; moribund state. All euthanasia procedures were performed using carbon dioxide inhalation followed by cervical dislocation, ensuring a swift and humane death. Specifically, the following criteria were used to confirm death: Cessation of respiratory movements: observing the complete absence of respiratory movements for at least 2 min; absence of heartbeat: palpating the chest to ensure the absence of a heartbeat; lack of corneal reflex: testing the corneal reflex by gently touching the cornea with a sterile object to ensure no blink response; confirmation of *rigor mortis*: observing the onset of rigor mortis as an additional confirmation. These steps ensured that the animals were humanely euthanized, and death was confirmed before proceeding with any further procedures.

X-Ray analyses. Fractures of anesthetized rats were radiographed for 6 s using an X-ray system (Kodak DirectView DR 3500; Kodak, Rochester, NY, USA) at 65 kV on days 0, 7, 14, 21, 28, and 42 to monitor the initial pin fixation and ongoing callus formation and resorption. Lane and Sandhu radiographic scoring (15) was used to compare the fracture healing between groups by two independent orthopedic surgeons. The development of the bone callus at the fracture end was examined using Image J (National Institutes of Health, Bethesda, MA, USA) and the average value of the maximal callus diameter on the frontal and lateral X-ray images was noted.

Micro-computed tomography. Bones were imaged at a resolution of 15 μm using a Scanco UCT 50 system (Scanco Medical, Brüttisellen, Zurich, Switzerland) operating at a peak voltage of 70 kV and 114 mA. A volume of interest was delineated, which encompassed the callus over a range of 3 mm between the distal and proximal end, and crossed all 200 sections, with contours of the volume of interest drawn

on sequential slices. With 3D software (3D-UCT Ray v. 3.8; Scanco Medical), the images were visualized as three-dimensional reconstructions. Using computed tomography analyzer software (UCT Tomography v. 6.3-4; Scanco Medical), the following values were obtained for the entire callus: bone volume (BV), total volume (TV), BV/TV, bone surface (BS), BS/BV, bone mineral density, trabecular thickness, trabecular separation, and trabecular number.

Mechanical testing. Rats were killed in a carbon dioxide chamber on days 21, 28, or 42 of the experiment, and the femurs were dissected to remove the fixators and any soft tissues. Mechanical testing was carried out in compliance with an earlier defined methodology (16). The femurs were centered on the osteotomy line and positioned on the supports, leaving a 20 mm free length between the bending supports for the bone. Material testing equipment (5,967 MicroTester; Instron, Norwood, MA, USA) was used to provide the load in 3-point bending at a deflection rate of 0.6 mm/min. Bending was performed at the osteotomy level in an anterior-posterior direction. The bones were maintained wet with a 0.9% NaCl solution throughout the testing. The callus was subjected to a bending force, which was continually monitored in relation to the sample deflection. Furthermore, a load-displacement diagram was captured, which allowed for the determination of the failure load. The area under the curve up to F-max was used to compute the work to failure, and linear regression was used to quantify stiffness. For both the experimental group and the control group, records of the failure load, stiffness, and work to failure were made for each femur.

Histological evaluation. Fractured limbs were removed and preserved for 24 h in 4% formalin, then for 1 to 2 months in a 10% ethylene-diaminetetraacetic acid (Sigma-Aldrich, St. Louis, MO, USA) solution to decalcify them before being embedded in paraffin for histological examination. To demonstrate the creation of cartilage, decalcified longitudinal slices were cut to a size of around 5 μm and stained with either Safranin O/Fast Green (Solabio, Beijing, PR China) or hematoxylin and eosin (Solabio). Five sections equally spaced from the first to the last slices were selected for examining the presence and characteristics of cartilage formation.

Immunohistochemistry for Ki-67. Samples that had been embedded in paraffin were sectioned, and the sections were rehydrated using water and graded ethanol. Sections were heated in a microwave for 3 min at 95˚C to recover antigen for antigen unmasking, after which they were chilled for 20 min at room temperature in 10 mM of sodium citrate buffer (pH 6.0). Sections were submerged in 3% H_2O_2 for 10 minutes to reduce endogenous peroxidase activity, followed by two 5-min washes in phosphate-buffered saline (PBS). Next, they were treated with 5% bovine serum albumin for 20 min at room temperature. After applying rabbit antibody to Ki-67 (1:400; ab15580; Abcam, Cambridge, MA, USA), the sections were left to incubate at 4˚C for an entire night. Following PBS washing, the specimens were incubated for 1 h at 37˚C with polyclonal biotinylated goat anti-rabbit secondary antibody (1:200; Boster Bio, Pleasanton, CA, USA), followed by 30 min at 37˚C with streptavidin-biotin complex. After three PBS washes, the slices were treated for 30 min with 3,3-diaminobenzidine substrate, and hematoxylin was used as a counterstain. All sections were photographed under a microscope at 400× magnification.

Detection of serum markers of bone formation and resorption. During the euthanasia of the rats, blood samples were obtained using heart puncture and allowed to stand at room temperature for a minimum of 30 min. The sera were separated using a centrifuge at 200×*g* for 10 min, and then kept at −20˚C. Serum bone-specific alkaline phosphatase (BALP), collagen type I alpha 1 chain (COL1A1), collagen type II alpha 1 chain (COL2A1), collagen type X (COL10), osteocalcin (bone gamma-carboxyglutamate protein, BGLAP), procollagen type I *N*-terminal propeptide (PINP), tartrate-resistant acid phosphatase and 5b (TRACP5b), and cross-linked C-telopeptide of type collagen (CTX) were measured using an enzyme-linked immunosorbent essay (ELISA) kit, rat PINP ELISA kit and rat CTX ELISA kit,

Table I. *Primer sequences.*

Target name	Forward primer (5'-3')	Reverse primer (5'-3')	Product size, bp
Actb	CACGATGGAGGGGCCGGACTCATC	TAAGACCTCTATGCCAACACAGT	240
Trap	ACGCCAATGACAAGAGGTT	TCACGGTGTCCAGCATAAAG	237
Balp	GAGTGCTGCCGTCCATTGTT	CAAGTCCTTGGCACGCTCTGT	133
Col1a1	CGAGTATGGAAGCGAAGGT	CAAGCGTGCTGTAGGTGAAT	227
Col2a1	ACGCTCAAGTCGCTGAACAA	TCAATCCAGTAGCTCCGCTCT	131
Col10	TTTCTGGGATGCCTCTTGTC	AATGGGATGGGAGCACCTAC	112
Bglap	GAGGGCAGTAAGGTGGTGAA	AACGGTGGTGCCATAGATGC	183
Egfr	GACAGGAGAACTGCCAGAA	GTAGCATTTATGGAGAGTG	435
Sox9	GACTCACATCTCTCCTAACG	CCTCTCGTTTCAGATCAA	183

Actb: β-Actin; *Balp*: serum bone-specific alkaline phosphatase; *Bglap*: bone gamma-carboxyglutamate protein, osteocalcin; *Col10*: collagen type X; *Col1a1*: collagen type I alpha 1 chain; *Col2a1*: collagen type II alpha 1 chain; *Egfr*: epidermal growth factor receptor; *Sox9*: box transcription factor 9; *Trap*: tartrate-resistant acid phosphatase.

respectively, from Elbscience (Wuhan, Hubei, PR China), as per the manufacturer's instructions.

qRT-PCR analysis. Within 3 mm of the proximal and distal fracture lines, total RNA was extracted from the callus using the TRIzol reagent (Aidlab, Beijing, PR China). SuperScript III (Invitrogen, Waltham, MA, USA) was then used to reverse transcribe the extracted RNA. Table I lists the primer sequences for the SYBR green Fast PCR system (Cytiva, Marlborough, MA, USA), which was used to conduct qRT-PCR.

Western blot analysis. In short, proteins were extracted from periosteal stem cells (PSCs) using RIPA lysis buffer, and their quantities were determined using a BCA assay kit (Thermo Fisher Scientific, Waltham, MA, USA). After that, the proteins were put on a polyvinylidene difluoride membrane and kept at 4˚C for incubation overnight with primary antibodies to SOX9, BGLAP, COL2A1, osteocalcin, Sp7 transcription factor (SP7), Runt-related transcription factor-2 (RUNX2), glucose transporter type 1 (GLUT1), hexokinase 2 (HK2), pyruvate dehydrogenase kinase 1 (PDK1), pyruvate kinase M2 (PKM2) and EGFR (Cell Signaling Technology, Danvers, MA, USA) at a dilution of 1:1,000; and glyceraldehyde 3-phosphate dehydrogenase (Abcam) at a dilution of 1:3,000. The membrane was exposed to the secondary antibody for 1 h at room temperature and was then developed using an enhanced chemiluminescence system (Thermo Fisher Scientific).

Cell isolation and culture. PSCs were isolated from intact femora and tibiae of 10-week-old rats. For the isolation of PSCs, femurs and tibias were carefully dissected free of muscle and connective tissue under sterile conditions. The epiphyses were protected from digestion by immersing them in 5% low melting point agarose (Invitrogen). Periosteal cells were then isolated by enzymatic digestion using 3 mg/ml collagenase II (Gibco, Grand Island, NY, USA) and 4 mg/ml dispase (Gibco) in α-minimum essential medium (α-MEM; Gibco) supplemented with 1% penicillin/streptomycin (Gibco). Cells from the first 10-min digestion were discarded, as they primarily contained residual muscle and connective tissue. PSCs were subsequently harvested after a 1-h digestion. The cell suspension was filtered through a 70 μm nylon mesh (BD Falcon; BD Biosciences, San Jose, CA, USA), washed twice, and cultured in α-MEM with 1% penicillin/streptomycin and 10% fetal bovine serum (FBS; Gibco) in a humidified incubator at 37˚C with 5% CO_2. All experiments were conducted using passage 2-3 PSCs.

Differentiation assays. The direction of PSCs differentiation plays a crucial role in fracture healing. To investigate the impact of gefitinib on PSCs differentiation, we adopted the

method of literature to simulate the effect of lipid environment on PSCs (17), we utilized lipid-reduced serum (LRS; Thermo Fisher Scientific) medium to simulate the differentiation milieu of PSCs in the fracture site. To evaluate chondrogenic differentiation, 150,000 PSCs were resuspended in 10 μl of control medium and seeded as micromasses at the center of a 24-well plate. After a 1-h incubation at 37˚C to allow cell attachment, 0.5 ml of FBS, LRS or LRS with 4 μM gefitinib medium containing 10 ng/ml recombinant human transforming growth factor-β1 (PHG9211; Gibco), 50 μM L-ascorbic acid 2-sulphate (Sigma-Aldrich), and 20 μM Rho kinase inhibitor Y-27632 (Sigma-Aldrich) was added to each well. The medium was refreshed every other day, and after 9 days, the micromasses were used for RNA or protein isolation.

Cell transfection. PSCs were seeded in six-well plates at a density of 2×10^5 cells/well and cultured in α-MEM supplemented with 10% FBS and 1% penicillin-streptomycin under standard conditions (37˚C, 5% CO_2) until they reached approximately 70-80% confluence. For *Sox9* plasmid transfection, 2 μg of the pcDNA3.1-SOX9 plasmid (V79020; Invitrogen) was diluted in 250 μl of Opti-MEM (Thermo Fisher Scientific) and mixed with 5 μl of Lipofectamine 3000 reagent (Invitrogen) in 250 μl of Opti-MEM. After a 5-min incubation at room temperature, the DNA-reagent complex was added to the cells which were then incubated for 6 h. The medium was then replaced with fresh α-MEM containing 10% FBS and 1% penicillin-streptomycin. For *SOX9* knockdown, PSCs were transfected with 20 nM of *Sox9*-specific siRNA using Lipofectamine RNAiMAX (Invitrogen). The siRNA (20 nM) was diluted in 250 μl of Opti-MEM, and 5 μl of Lipofectamine RNAiMAX in 250 μl of Opti-MEM was added. The siRNA-Lipofectamine complex was incubated for 20 min at room temperature before being added to the cells. After 6 h of incubation, the medium was replaced with fresh α-MEM containing 10% FBS and 1% penicillin-streptomycin. The transfection efficiency for both plasmid and siRNA was evaluated by qPCR analysis at 48 h post-transfection. PSCs were then harvested for downstream analysis at 48 h post-transfection. The *Sox9* siRNA target sequence was as follows: 5'- GCGACAACTTTACCAGTTTCAGT-3'. *SOX9* siRNA and non-targeted siRNA were purchased from RiboBio (Guangzhou, PR China).

Metabolic reprogramming assays. Glucose uptake assay*:* A glucose uptake colorimetric test kit (Abcam) was used to measure glucose uptake. After being transfected with the chosen vector and plated in a 6-well plate, the cells were cultured for 24 h. After transfected cells were gathered, the number of cells was determined. A 96-well cell culture plate was then seeded with 1×10^4 cells and was incubated at 37˚C overnight. The cells were deprived of glucose for 2 h the next day. After 40 min of incubation with 100 μl Krebs-HEPES, each well received 10 μl of 10 mM 2-deoxy-D-glucose, and was then incubated for 20 min. After that, the cells were harvested utilizing extraction buffer, and the absorption of glucose was tested. The optical density was used to measure glucose absorption at a wavelength of 412 nm.

Lactate and adenosine triphosphate (ATP) production assay: Lactate production was measured using an L-lactate assay kit (colorimetric method, Abcam). Transfected cells were seeded in a 96-well cell culture plate and incubated overnight at 37˚C. After treatment, the culture medium was collected for lactate measurement. For lactate determination, L-lactate assay kit (colorimetric method, Abcam) was used according to the manufacturer's protocol. Briefly, 50 μl of culture supernatant was added to the assay well, and the lactate reagent was mixed with the sample. The absorbance at 570 nm was measured using a microplate reader. ATP levels were quantified using a commercial ATP assay kit (Abcam), following the manufacturer's instructions. The resulting luminescence was measured using a luminometer, and ATP levels were normalized to protein concentration to assess metabolic activity.

Extracellular acidification rate (ECAR) assay: Seahorse XF glycolysis stress test kit (Agilent Technologies, Santa Clara,

CA, USA) and Seahorse XF Cell Mito Stress Test Kit (Agilent Technologies) were used to determine ECAR and extracellular acidification rate [by measuring the oxygen consumption rate (OCR)], respectively. The transfected and gefitinib-treated PSCs were cultured for overnight at 37˚C in a 96-well plate supplemented with 10% FBS. For the purpose of measuring ECAR, glucose (10 mM), oligomycin (1 μM), and 2-deoxy-D-glucose (50 mM) were successively introduced to each well after baseline measurements were made. For OCR determination, rotenone (2 μM), antimycin A (2 μM), oligomycin (1 μM), and carbonyl cyanide 4-(trifluoromethoxy)phenylhydrazone (1 μM) were introduced in that order. Seahorse XF-96 Wave software (Agilent Technologies) was used to analyze the findings.

*Mitochondrial function and fatty acid oxidation (FAO) a*ssay: FAO was assessed by measuring the OCR in the presence of palmitate (30 μM). PSCs were seeded onto a 96-well XF96 type plate (Agilent Technologies) and incubated at 37˚C overnight. Prior to measurement, the cells were incubated for 1 h at 37˚C without CO_2 in XF Assay Modified DMEM culture medium (1 g/ml glucose, pH 7.4; Seahorse Biosciences), replacing the whole mixture. Etomoxir (Sigma-Aldrich) was added at a final concentration of 0.1 mM. Fatty acid-linked OCR was measured following the sequential addition of oligomycin (1 μM), 4 (trifluoromethoxy) phenylhydrazone (1 μM), rotenone (2 μM), and antimycin A (2 μM) to achieve the indicated final concentrations. Measurements were performed according to the kit protocol for FAO. Seahorse XF-96Wave software was used to analyze the results.

Dual luciferase reporter gene assay. To assess the transcriptional activity of *Sox9* and its downstream target genes, dual luciferase reporter gene assays were performed. PSCs were seeded in 96-well plates and transfected with either the pGL3 control plasmid (Promega, Madison, WI, USA) or the pGL3-3-*Sox9* reporter construct, which contains the *Sox9* promoter region driving the firefly luciferase gene. After 24-48 hof treatment with gefitinib or vehicle, the cells were harvested for luciferase activity measurement. Renilla luciferase activity was used as an internal control for normalization. The dual luciferase assay was carried out using the Dual-Luciferase Reporter Assay System (Promega) according to the manufacturer's instructions. The activity of firefly luciferase was measured using a Luminoskan Ascent luminometer (Thermo Fisher Scientific), and relative luciferase activity was calculated by normalizing firefly luciferase activity to Renilla luciferase activity. In addition, PSCs were transfected with reporter constructs containing the pGL3 vector coupled to the promoters of *Glut1*, *Pdk1*, *Hk2*, and *Pkm2*, which are known downstream targets of *Sox9*. The cells were then treated with gefitinib or vehicle. Luciferase activity was measured, and the relative activity of the reporter constructs was calculated to assess the impact of *Sox9* on the transcription of these target genes under gefitinib treatment.

Statistical analysis. The mean±standard deviation of measurements made independently at least three times is used to represent findings. To assess the statistical difference between the control and treatment groups, Student's *t*-test was used. Statistical tests were conducted with SPSS software 19.0 (IBM Corp., Armonk, NY, USA), with a significance level of $p<0.05$. One-way analysis of variance test or Student's *t*-test was used to compare the mean values across the groups of rats at various intervals.

Results

Gefitinib enhances radiographic behavior in bone fracture. Radiographic images and Lane and Sandhu radiographic scoring were utilized to assess the impact of gefitinib on bone fracture characteristics (Figure 1). The analysis of callus diameter and radiographic scoring revealed that the gefitinib-treated group exhibited a smaller callus diameter but superior radiographic scores compared to the control group from day 7 to day 21 (Figure 1A and B). Notably, by day 14, the gefitinib-treated group displayed more pronounced callus formation and a closely apposed,

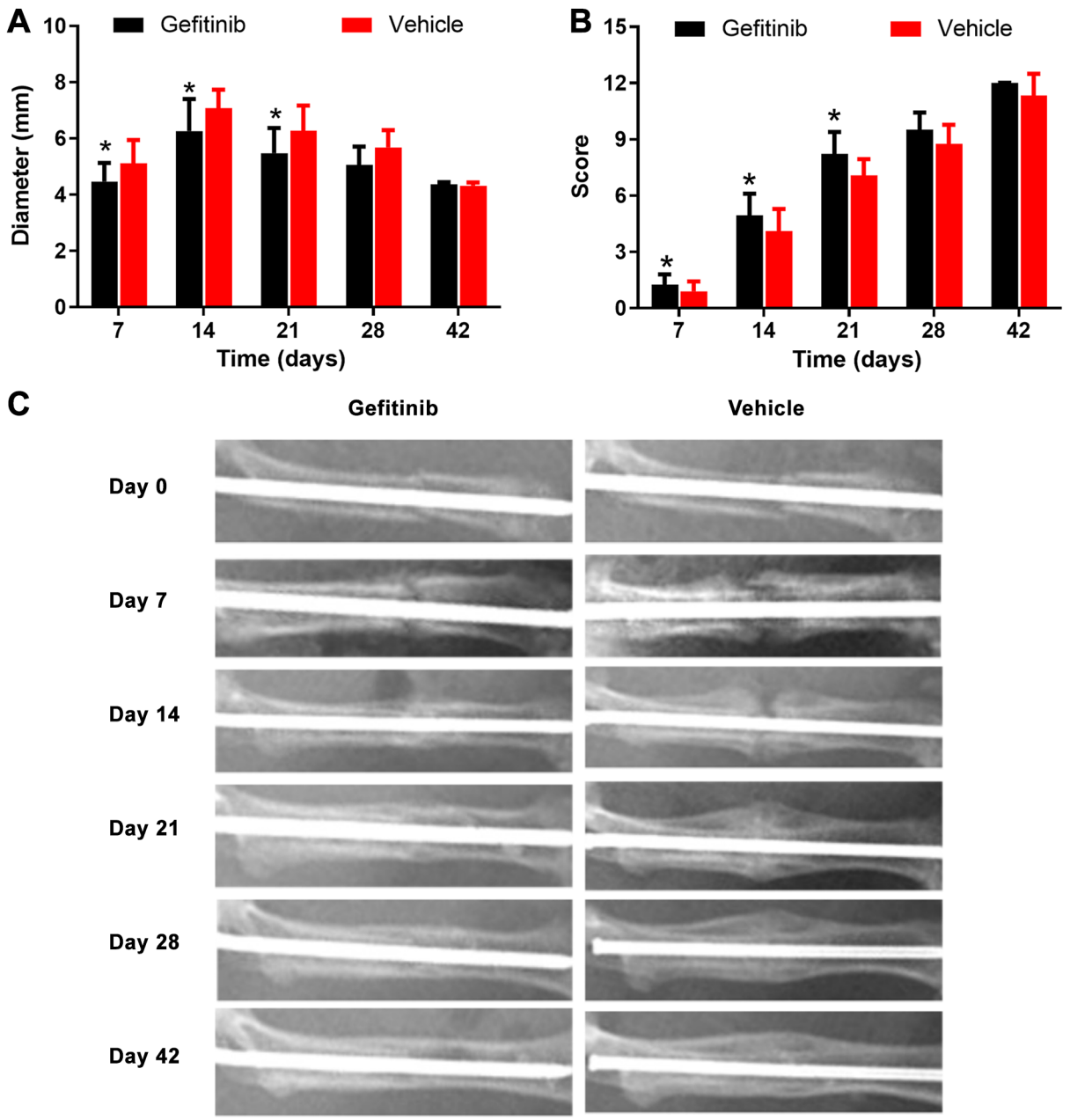

Figure 1. *Gefitinib improves radiographic measures related to bone fracture. (A) The diameter of the callus during fracture healing. (B) The Lane and Sandhu radiographic score during fracture healing. (C) Radiographs were conducted on before and after surgery to observe pin fixation, confirm fracturing, and monitor callus formation. Radiographic images showed fracture healing was promoted and callus resorption increased in the gefitinib-treated rats. *Significantly different at p<0.05. Data are the mean±standard deviation of three rats.*

indistinct fracture line, whereas the fracture line in the control group remained visible (Figure 1C). Remarkably, by day 21, both groups showed reduced callus formation, with the gefitinib-treated group exhibiting an obscured fracture line. These findings strongly suggest that gefitinib enhances radiographic scoring in bone fracture cases.

Table II. *Bone-healing parameters in gefitinib-treated and control groups during fracture healing.*

Parameter	Time point	Gefitinib-treated group (n=3)	Control group (n=3)	*p*-Value
TV (mm^3)	14 d	97.40±8.24	88.76±10.01	0.231
	21 d	78.69±4.51	77.40±13.11	0.859
	28 d	109.33±16.47	114.19±18.19	0.705
	42 d	67.27±7.21	89.72±17.59	0.056
BV (mm^3)	14 d	59.30±6.54	42.39±7.82	**0.016**
	21 d	43.08±2.33	33.43±5.94	**0.023**
	28 d	58.12±9.10	49.03±5.74	0.142
	42 d	35.73±4.83	41.64±2.04	0.065
BV/TV (%)	14 d	0.6098±0.0575	0.4781±0.0676	**0.025**
	21 d	0.5493±0.05172	0.4373±0.0748	**0.049**
	28 d	0.5326±0.0437	0.4324±0.0342	**0.011**
	42 d	0.5321±0.0574	0.4749±0.0720	0.260
TBN (1/mm)	14 d	2.045±0.114	1.630±0.213	**0.014**
	21 d	1.858±0.184	1.323±0.209	**0.009**
	28 d	2.039±0.257	1.653±0.080	**0.028**
	42 d	1.046±0.146	1.097±0.214	0.708
TBTh (mm)	14 d	0.3334±0.0217	0.2697±0.0343	**0.020**
	21 d	0.3275±0.0310	0.2797±0.0197	**0.040**
	28 d	0.2690±0.0234	0.2300±0.0171	**0.036**
	42 d	0.6037±0.1749	0.4119±0.1131	0.115
TBSp (mm)	14 d	0.2402±0.0381	0.2239±0.0477	0.612
	21 d	0.3919±0.0735	0.2950±0.0258	**0.047**
	28 d	0.2694±0.0767	0.2469±0.0503	0.640
	42 d	0.5504±0.0972	0.5267±0.0990	0.743
BS (mm^2)	14 d	391±49.9	389±105.9	0.972
	21 d	336±47.3	314±48.6	0.540
	28 d	390±48	360±58.6	0.464
	42 d	213±64.6	186±24.3	0.466
BS/BV (mm^{-1})	14 d	9.39±1.66	6.51±1.42	**0.039**
	21 d	10.15±1.14	7.33±1.31	**0.017**
	28 d	7.99±0.81	6.24±0.79	**0.021**
	42 d	5.10±1.47	5.35±1.37	0.810
BMD (mgHA/cm)	14 d	605±52.4	593±75.5	0.792
	21 d	611±42.1	620±26.2	0.740
	28 d	612±37.8	659±26.1	0.088
	42 d	686±21.6	723±7.4	**0.018**

BMD: Bone mineral density; BV: bone volume; BS: bone surface; HA: hydroxyapatite; TBN: trabecular number; TBSp: trabecular separation; TBTh: trabecular thickness; TV: total volume.

Gefitinib contributes to better microstructure and callus quality of the femur. As illustrated in Table II, while there was no discernible disparity in TV, the gefitinib group exhibited notably higher values of BV and BV/TV compared to the control group on days 14 and 21. Moreover, TBN and TBTh were significantly greater in the gefitinib-treated group on days 14, 21, and 28, with an elevated trabecular separation observed on day 21. Additionally, BS/BV values were consistently higher in the gefitinib group on days 14, 21, and 28. Furthermore, MCT analysis revealed a significantly higher bone mineral density in the gefitinib-treated group compared to the control group. Cross-sectional MCT images depicted enhanced bone healing in the gefitinib-treated group, characterized by predominantly trabecular bone formation with reduced presence of immature non-osseous tissue. Notably, 3D imaging indicated markedly superior healing in rats administered gefitinib at each observation point except on day 42 (Figure 2A).

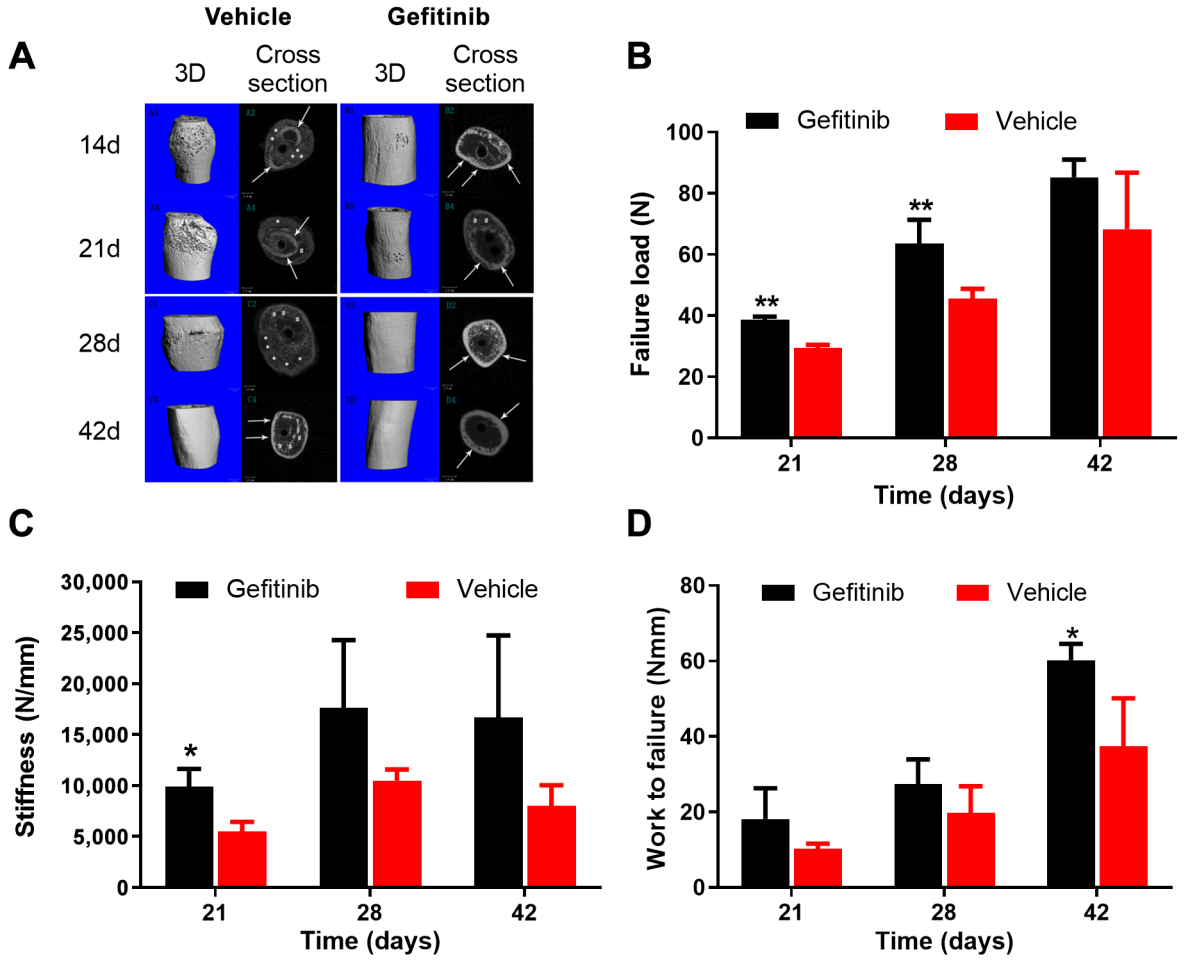

Figure 2. *Gefitinib is associated with better microstructure and callus quality of repaired femoral fracture. (A) Cross-sectional and 3-dimensional micro-computed tomography images of rat femurs in the control and the gefitinib-treated groups on days 14, 21, 28 and 42 after fracture. Load (B), stiffness (C) and work to failure (D) during fracture healing. Data are expressed as the mean±standard deviation of three rats. Significantly different from the vehicle-treated control at: *p<0.05, and **p<0.01.*

Biomechanical testing, encompassing assessment of failure loads, stiffness, and work to failure, was utilized to evaluate the impact of gefitinib on femoral callus quality. Results of failure load tests showed the gefitinib-treated group exhibited significantly greater strength compared to the control group on days 21 and 28 (Figure 2B). Additionally, the stiffness of rat bones in the gefitinib-treated group demonstrated notable enhancement relative to the control group on day 21 (Figure 2C). Moreover, the work to failure measure in the gefitinib-treated group surpassed that of the control group on day 42 (Figure 2D). Collectively, these outcomes suggest that gefitinib contributes to superior callus quality in femoral healing processes.

Gefitinib is associated with better histomorphological and immunohistochemical scores. To morphologically confirm the effect of gefitinib on fracture healing, callus and fracture healing were investigated with hematoxylin and eosin staining. As depicted in Figure 3A, by day 7, the fracture gap in the gefitinib-treated group appeared less conspicuous compared to the control group, where the gap

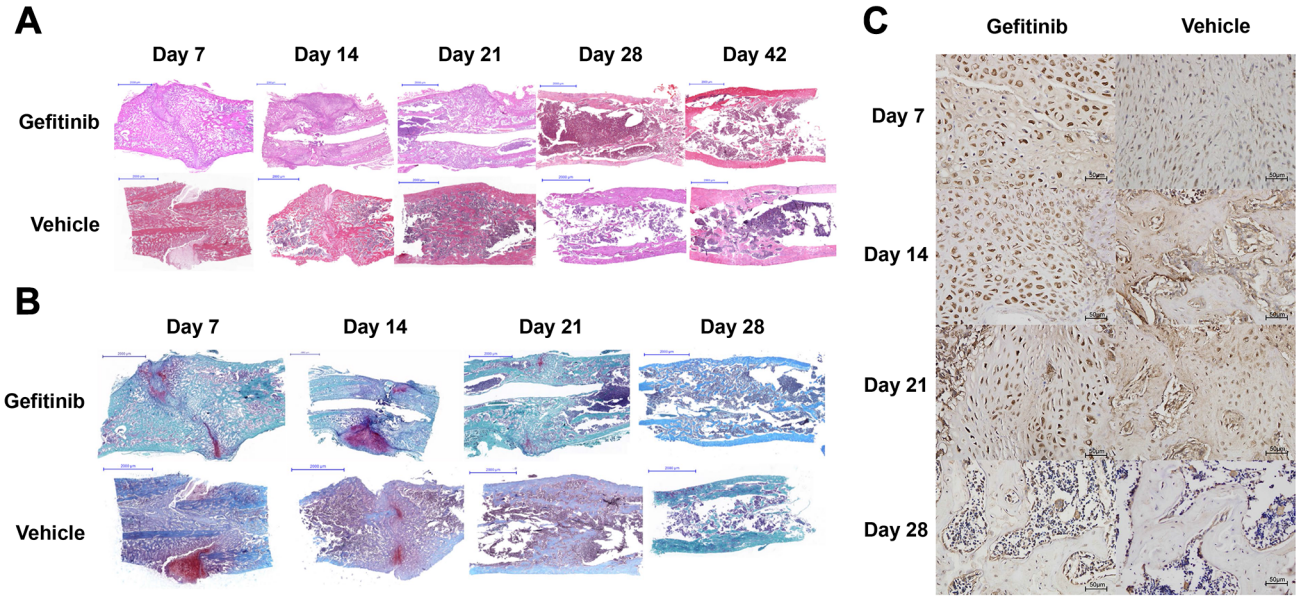

Figure 3. *Gefitinib is associated with better histomorphological and immunohistochemical measures during healing of femoral fracture. One-month-old rats were treated daily with either gefitinib or vehicle and healing was evaluated every 7 days after surgery. (A) Histological images (hematoxylin and eosin staining) of the bone fracture sites at each time point. Scale bars=2,000 μm. (B) Safranin O/Fast Green staining of the bone fracture sites at each time point. Scale bars=2,000 μm. (C) Ki-67^{+} proliferative cells at each time point. Scale bars=50 μm.*

was still discernible. Furthermore, by day 14, the extent of callus formation in the gefitinib-treated group was notably greater than that in the control group. Additionally, as illustrated in Figure 3B, Safranin O/Fast Green staining revealed that gefitinib treatment resulted in a less pronounced blue coloration compared to the control group, indicating a reduced accumulation of extracellular matrix components compared to the control group. Furthermore, gefitinib administration led to an increased presence of Ki-67^{+} proliferative cells on days 7, 14, and 21 (Figure 3C). Taken together, these findings suggest that gefitinib is associated with improved histomorphological and immunohistochemical characteristics.

Gefitinib modulates gene expression patterns and serum bone markers in bone healing. We aimed to determine the effect of gefitinib on the gene expression associated with fracture healing. The analysis showed that markers of bone formation, *Balp, Col2a1, Col2a1, COL10* and osteocalcin were generally upregulated from days 7 to 28 and reached peak levels on day 21. *Balp*, *Col2a1*, *Col10*, and osteocalcin were generally upregulated in the gefitinib-treated group compared to the vehicle-treated group, with significant increases observed at specific time points (notably at 21 and 14 days for COL10 and osteocalcin). As a bone resorption marker, tartrate-resistant acid phosphatase (*Trap)* was upregulated in the gefitinib-treated group between day 7 and day 21 compared with the control group (Figure 4A).

Serum levels of osteogenic markers were also assessed, revealing noteworthy differences. Specifically, serum levels of BALP and PINP in the gefitinib-treated group were significantly elevated compared to the control group on days 7, 14, and 21 post-operation. In the gefitinib-treated group, levels of these reached their peak on day 21: In contrast, in the control group, the levels peaked on day 28. Additionally, serum levels of TRACP 5b and CTX in the gefitinib-treated group exhibited an increase relative to the control group, albeit only on day 7 (Figure 4B).

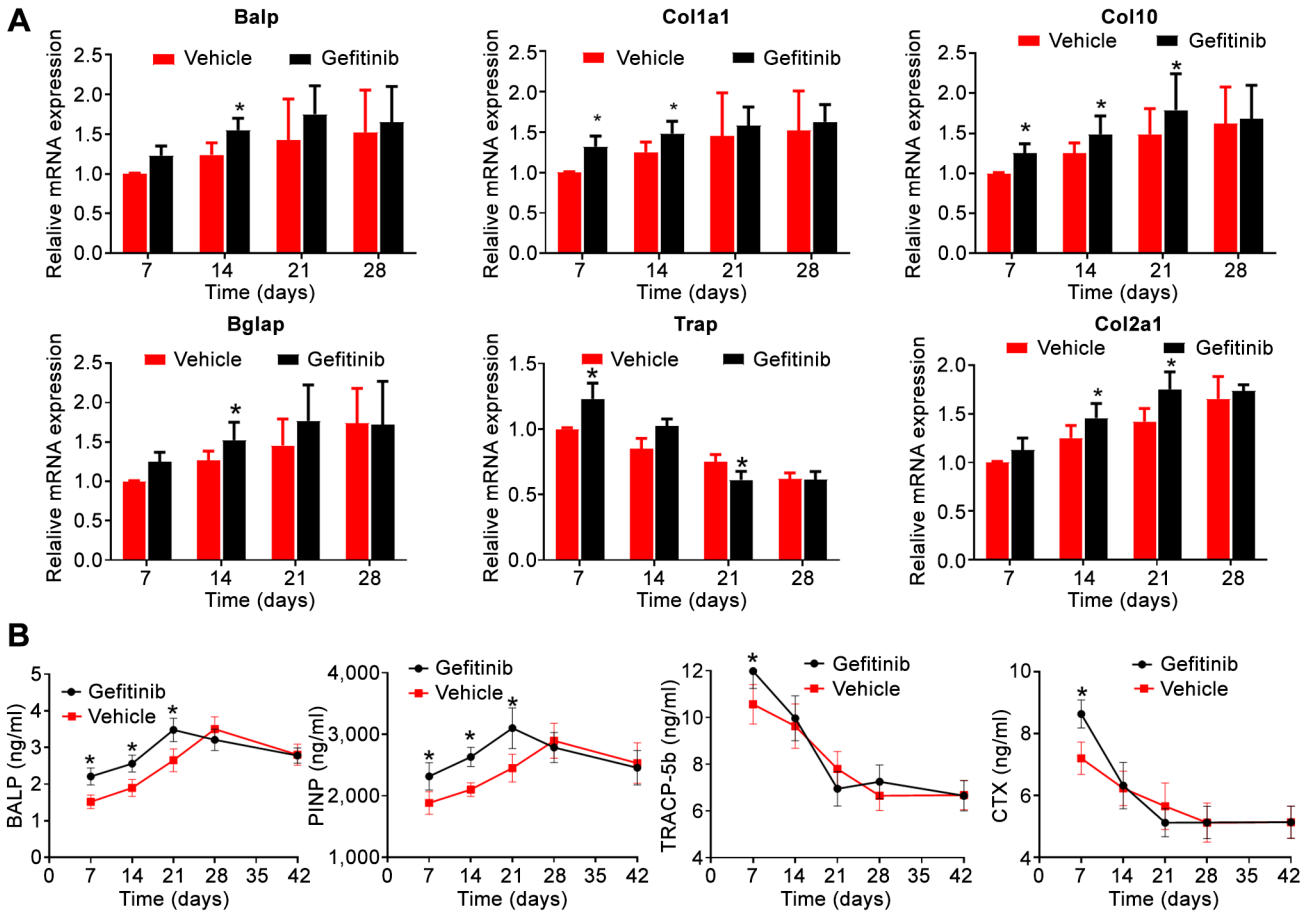

Figure 4. *Gefitinib modulates gene-expression patterns and serum bone turnover markers in bone healing. (A) The expression of bone-specific alkaline phosphatase (Balp), collagen type I alpha 1 chain (Col1a1), collagen type X (Col10), collagen type II alpha 1 chain (Col2a1), bone gamma-carboxyglutamate protein (Bgalp), and tartrate-resistant acid phosphatase (Trap) mRNA in gefitinib-treated and control-treated rats after the fracture. Quantitative representations of multiple results are expressed as values relative to the minimum value of the control group. (B) The serum levels of bone turnover markers: osteogenic markers [BALP and procollagen type I N-terminal propeptide (PINP)] and osteoclastic markers (tartrate-resistant acid phosphatase and 5b (TRACP-5b) and cross-linked C-telopeptide of type collagen (CTX)]. Data are expressed as the mean±standard deviation of three rats. *Significantly different at p<0.05 vs. the control on the same day.*

Gefitinib regulates the differentiation of PSCs by targeting Sox9. The direction of PSC differentiation plays a crucial role in fracture healing. To investigate the impact of gefitinib on PSC differentiation through targeting *Sox9*, we adopted the method of literature to simulate the effect of a lipid environment on PSC (17), we utilized LRS to simulate the differentiation milieu of PSCs in the fracture site with treatment with gefitinib and transfection with *Sox9*. Our findings demonstrate that LRS treatment significantly enhanced PSC differentiation towards chondrogenesis while attenuating osteogenic differentiation (Figure 5A). Specifically, the expression levels of osteoblast markers such as *Bgpal*, *Runx2*, and *Sp7* decreased, whereas those of chondrocyte markers Aggrecan, *Col2a1*, and *Sox9* significantly increased (Figure 5B and C). Importantly, gefitinib administration effectively reversed the LRS-induced changes in cell differentiation patterns (Figure 5A-C).

Following LRS treatment, both mRNA and protein levels of EGFR and SOX9 were upregulated, as evidenced by our observations (Figure 5D and E). Notably, gefitinib

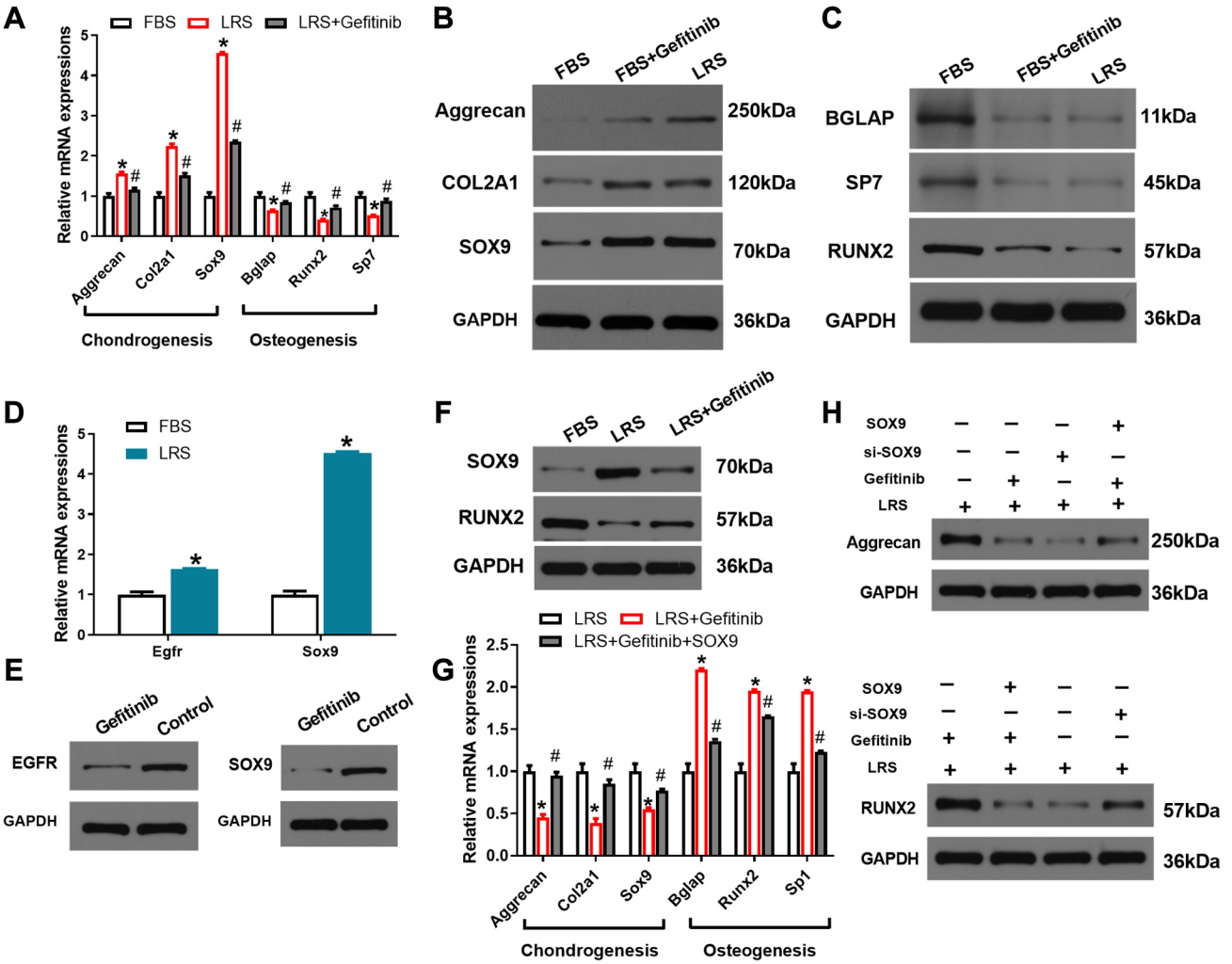

Figure 5. *Gefitinib regulated the differentiation of periosteal stem cells (PSCs) by targeting SRY-box transcription factor 9 (Sox9). (A) The mRNA expression of osteoblast marker bone-specific alkaline phosphatase (Bglap), Runt-related transcription factor-2 (Runx2), and Sp7 transcription factor (Sp7) decreased, while the expression of chondrocyte marker aggrecan, collagen type II alpha 1 chain (Col2a1), and Sox9 increased. *Significantly different from the fetal bovine serum (FBS) group at p<0.05. #Significantly different from the lipid-reduced serum (LRS) + gefitinib group at p<0.05. (B, C) The protein expression of osteoblast marker BGLAP, RUNX2, and decreased, while the expression of chondrocyte marker aggrecan, COL2A1, and SOX9 increased. (D) After lipid-reduced serum (LRS) treatment, the expression of epidermal growth factor receptor (Egfr) and Sox9 increased at the mRNA level. *Significantly different from the FBS group at p<0.05. (E) After treatment with LRS, the expression of EGFR and SOX9 increased at the protein level. (F) Gefitinib reversed the increase of SOX9 expression and reduced osteoblast differentiation induced by LRS. (G, H) LRS induced cartilage differentiation and reduced osteogenic differentiation, whilst gefitinib reversed the effect of LRS, resulting in reduced chondrocyte differentiation and increased osteoblast differentiation. The overexpression of Sox9 partially counteracted these effects of gefitinib. GAPDH: Glyceraldehyde-phosphate dehydrogenase. Significantly different at p<0.05 from: *LRS group; #LRS+gefitinib group.*

intervention reversed the upregulation of SOX9 expression induced by LRS and mitigated the decrease in osteoblastic differentiation (Figure 5F). Furthermore, through rescue experiments, we confirmed that gefitinib counteracted the effects of LRS, resulting in reduced chondrogenic differentiation and increased osteoblastic differentiation, whereas overexpression of *Sox9* partially reversed the effects of gefitinib (Figure 5G and H). These

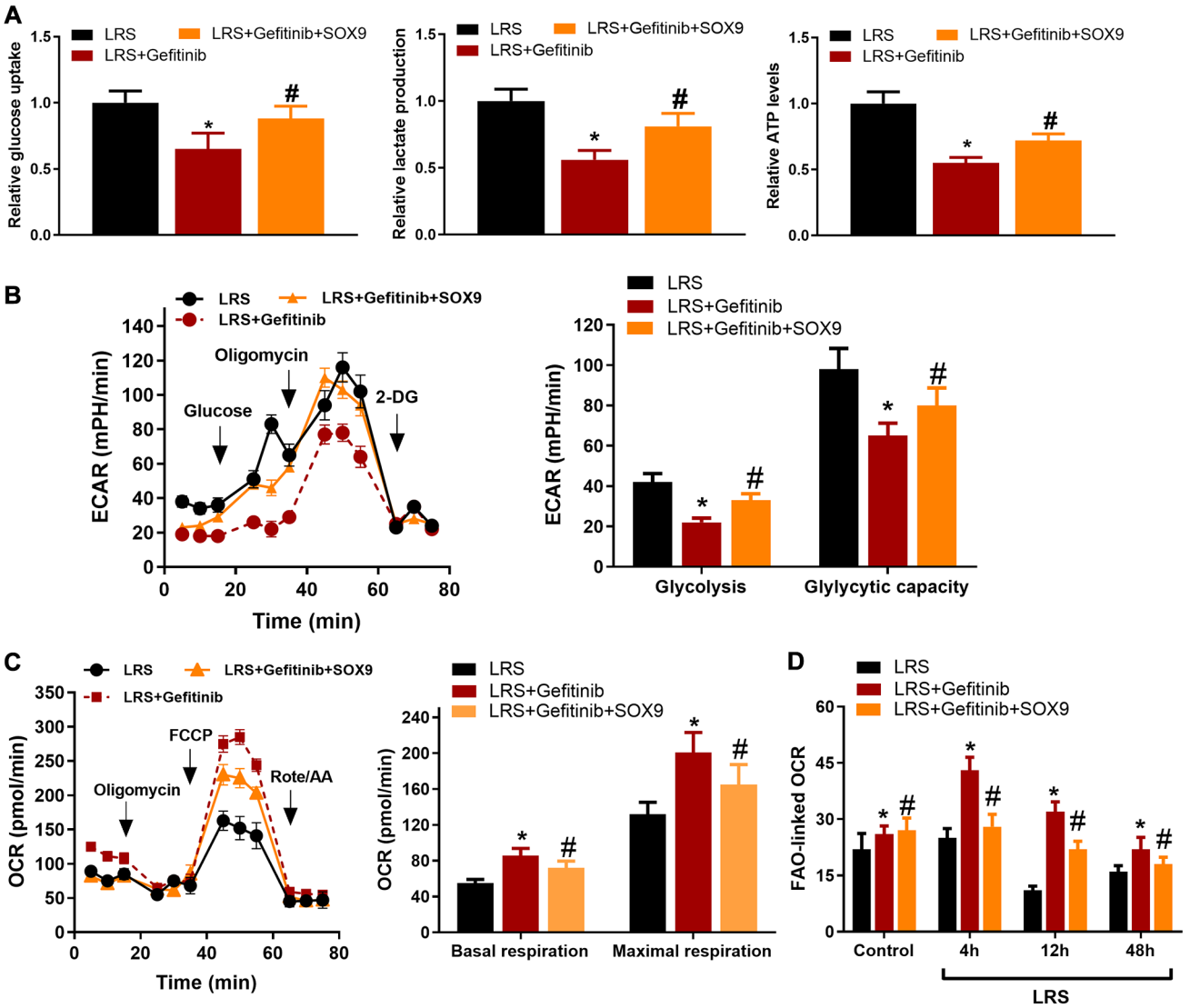

Figure 6. *Gefitinib reversed the metabolic reprogramming of periosteal stem cells (PSCs) by inhibiting box transcription factor 9 (Sox9). (A) Gefitinib inhibited glucose uptake, lactic acid production, and adenosine triphosphate (ATP) production after treatment with lipid-reduced serum (LRS). (B) The extracellular acidification rate (ECAR) assay showed that gefitinib reduced glycolytic capacity and glycolysis under LRS treatment. (C) The oxygen consumption rate (OCR) assay showed that gefitinib increased the OCR, raised the basal mitochondrial level and maximum mitochondrial level, and promoted oxidative phosphorylation; this effect of gefitinib was reversed by Sox9 overexpression. (D) Gefitinib increased fatty acid oxidation (FAO), which was also reversed by Sox9 overexpression. Significantly different at p<0.05 from: *LRS group; #LRS+gefitinib group. AA: Antimycin A; 2-DG: 2-Deoxy-D-glucose; FCCP: carbonyl cyanide 4-(trifluoromethoxy)phenylhydrazone; Rote: rotenone.*

results collectively suggest that the EGFR pathway acts upstream of SOX9 and forms an axis that drives PSCs towards chondrocytic differentiation in the fracture microenvironment, consequently delaying fracture healing.

Gefitinib reverses the metabolic reprogramming of PSCs by inhibiting SOX9. Recent investigations have uncovered the pivotal role of *Sox9*-driven metabolic reprogramming in the differentiation of PSCs during fracture healing (17). To elucidate the impact of gefitinib on the metabolic

reprogramming of PSCs through targeting *Sox9*, we evaluated glycolysis, oxygen consumption, and FAO in PSCs treated with LRS and transfected with *Sox9*. The results suggest that gefitinib inhibited glucose uptake, lactic acid production, and ATP production after LRS treatment (Figure 6A). Furthermore, ECAR results suggest that gefitinib reduced both the glycolytic capacity and glycolytic potential under LRS conditions (Figure 6B). Notably, the inhibitory effect of gefitinib on glycolysis was reversed by overexpression of *Sox9*. Similarly, OCR assays demonstrated that gefitinib enhanced levels of OCR, basal and maximum mitochondrial activity, thereby promoting oxidative phosphorylation metabolism. Again, this effect of gefitinib can be counteracted by *Sox9* overexpression (Figure 6C). Additionally, gefitinib augmented FAO metabolism, as evidenced by increased oxygen consumption related to FAO and oxidative phosphorylation of palmitic acid. Once more, the inhibitory effect of gefitinib on FAO was reversed by *Sox9* overexpression (Figure 6D). These findings collectively suggest that gefitinib reverses the metabolic reprogramming of PSCs by inhibiting *Sox9*.

Gefitinib inhibits metabolic reprogramming by inhibiting Sox9 transcription and Sox9-controlled metabolic reprogramming-associated target genes. Our results indicated that gefitinib inhibited the transcription of *Sox9*, leading to reduced expression levels of *Sox9* mRNA and protein in PSCs, as evidenced by RT-PCR and western blotting assays, respectively (Figure 7A and B). Furthermore, gefitinib treatment did not affect its stability but reduced transcriptional activity of *Sox9* mRNA, as demonstrated by mRNA decay (Figure 7C) and dual luciferase reporter gene assays (Figure 7D). Additionally, gefitinib reduced the expression of metabolic reprogramming-associated proteins, including GLUT1, PDK1, HK2 and PKM2, in PSCs, as determined by western blotting (Figure 7E). For further investigation of *Sox9* activity, a dual luciferase reporter assay was also used to measure the transcriptional activity of downstream targets of *Sox9*, namely *Glut1, Pdk1, Hk2*, and *Pkm2* in PSCs after treatment with gefitinib and/or *Sox9*. Dual luciferase reporter gene assays revealed that gefitinib diminished the transcription of *Glut1* and *Pdk1* of *Sox9* in PSCs (Figure 7F). These findings collectively suggest that gefitinib attenuates metabolic reprogramming by targeting the transcription of *Sox9* and its downstream effectors in PSCs. Collectively, gefitinib facilitates bone fracture healing by suppressing the EGFR signaling pathway and mitigating aberrant *Sox9*-driven bone metabolic reprogramming (Figure 8).

Discussion

Bone healing is a multifaceted process that involves both callus formation and endochondral ossification. Typically, the process of endochondral ossification during fracture healing is subdivided into several distinct stages, including hematoma formation, acute inflammation, granulation tissue formation, callus formation, and ultimately bone remodeling. It is important to recognize that bones are dynamic organs undergoing continuous remodeling, a process meticulously orchestrated by osteoclasts, osteoblasts, and osteocytes (8). Indeed, research has underscored the significance of EGFR signaling as a key pathway in the regulation of bone metabolism. This signaling cascade plays a crucial role in governing the proliferation and differentiation of both osteoblasts and chondrocytes, highlighting its pivotal involvement in bone formation and maintenance processes (18). However, there are limited data on the underlying molecular mechanisms by which EGFR contributes to the development of bone fracture healing.

Effective fracture healing necessitates several key factors, including mechanical stability, the presence of osteogenic cells, an osteoconductive scaffold, optimal growth factor signaling, and adequate vascularization (19). Thus, adequate systemic and local conditions are required to ensure uneventful fracture consolidation. In the present study, we found that gefitinib, which has been approved by the US Food and Drug Administration for lung cancer treatment, exhibits the capacity to augment bone fracture mending while modulating dysregulated bone metabolism.

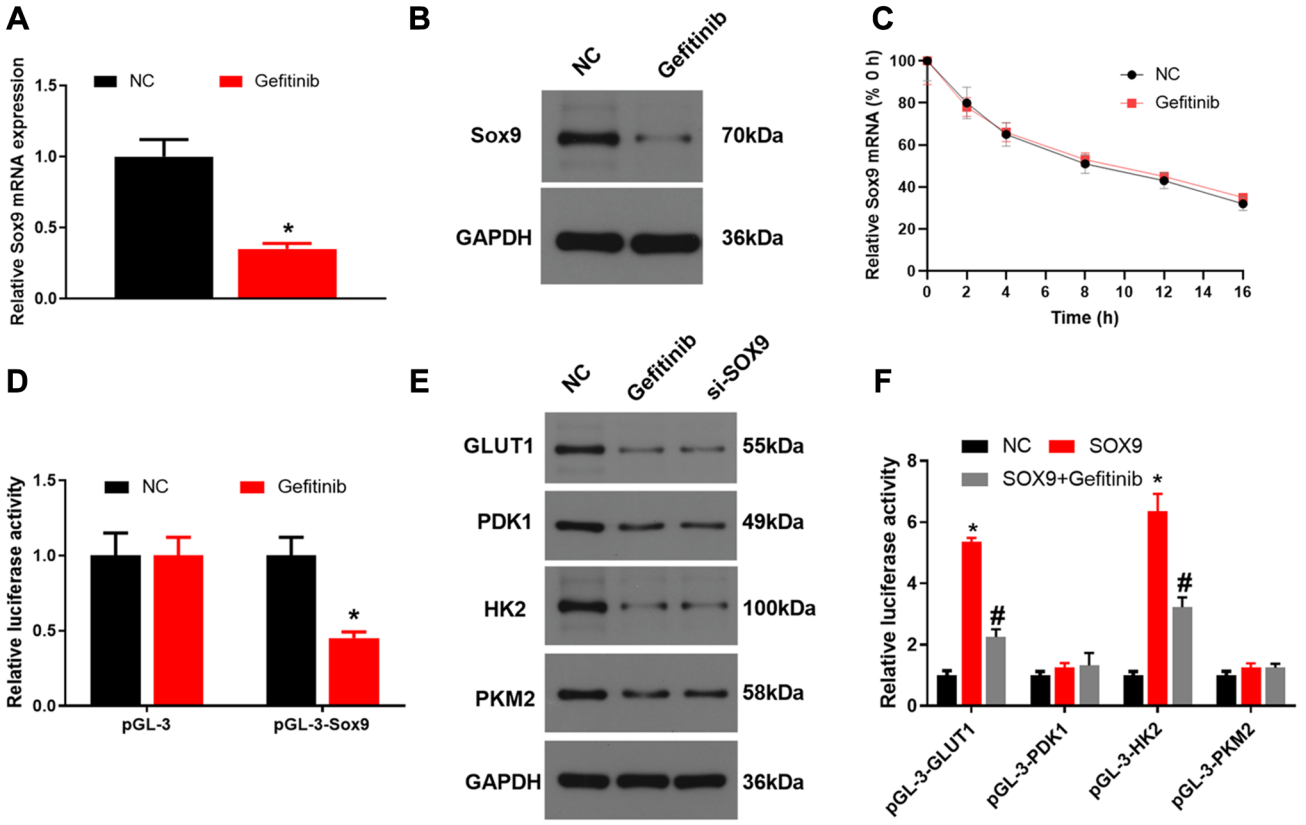

Figure 7. *Gefitinib inhibits metabolic reprogramming by inhibiting SRY-box transcription factor 9 (Sox9) transcription and downstream targets. (A) Quantitative real-time polymerase chain reaction was used to detect the effect of gefitinib on box transcription factor 9 (Sox9) mRNA in periosteal stem cells (PSCs). (B) Western blot was used to detect the effect of gefitinib on SOX9 protein in PSC cells. (C) Using the mRNA decay method, the effect of gefitinib on the stability of Sox9 mRNA in PSC cells was determined. (D) Dual luciferase reporter gene assay was used to detect the effect of gefitinib on Sox9 mRNA transcriptional activity in PSC cells. (E) Western blot method was used to detect the effect of gefitinib on proteins associated with metabolic reprogramming in PSCs. (F) Dual luciferase reporter gene assay was used to detect the effect of gefitinib on the transcription of Sox9 downstream targets, namely glucose transporter type 1 (Glut1), hexokinase 2 (Hk2), pyruvate dehydrogenase kinase 1 (Pdk1), pyruvate kinase M2 (Pkm2), in PSC cells. NC: Negative control. Significantly different at $p<0.05$ from: *NC group; #SOX9 group.*

In our investigation, initial X-ray examination and radiographic scoring revealed that the group treated with gefitinib exhibited a reduced callus diameter but demonstrated superior radiographic scores. Specifically, X-ray imaging demonstrated a more conspicuous callus formation in the gefitinib-treated group, characterized by a closely approximated and indistinct fracture line on day 21. Moreover, the callus formation in both experimental groups diminished over time, yet the gefitinib-treated group displayed a higher density at the fracture site, suggesting an amelioration in radiographic characteristics associated with bone fracture owing to gefitinib administration.

Furthermore, MCT revealed a higher proportion of bone tissue formation, specifically woven bone, within the callus, indicating an enhanced state of healing. Notably, the group administered gefitinib exhibited superior trabecular BV and architecture, corroborating the role of gefitinib in fostering woven bone formation and recuperation. Additionally, immunohistochemistry demonstrated enhanced histomorphological and immunohistochemical outcomes associated with gefitinib administration. Notably, immunohistochemical analysis revealed heightened cell proliferation during the initial healing phase, particularly evident in chondrocytes and

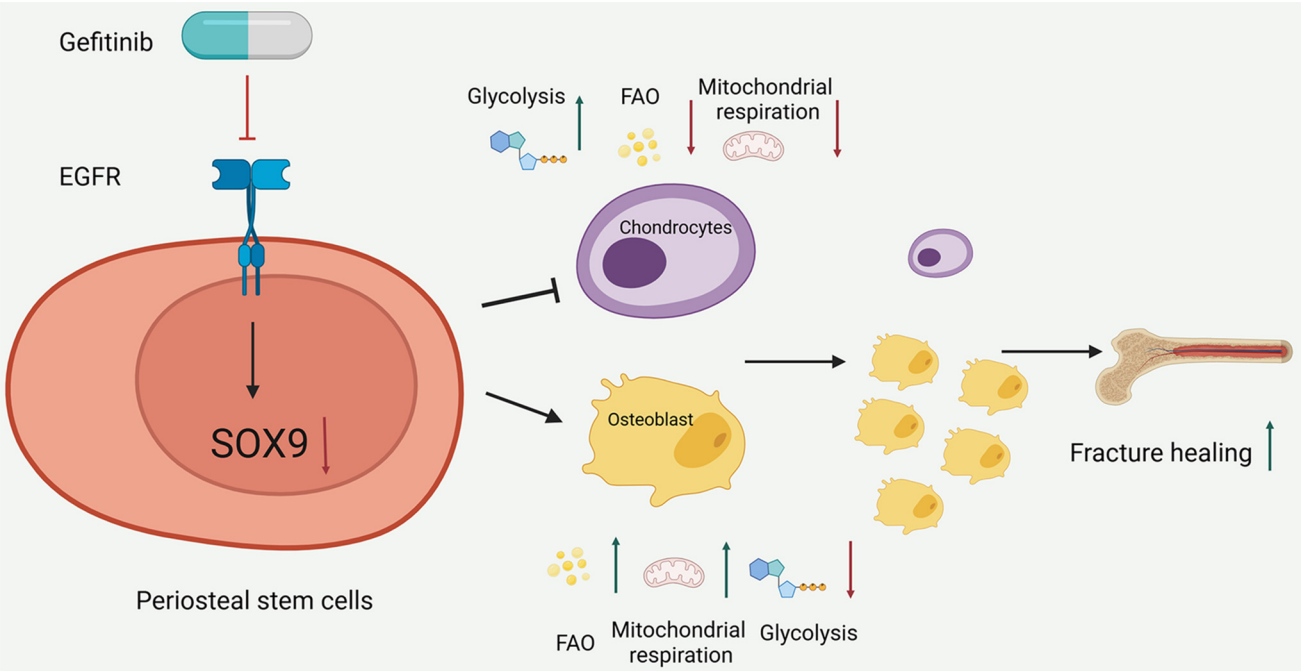

Figure 8. *Gefitinib facilitates bone fracture healing via inhibiting epidermal growth factor receptor (EGFR) signaling pathway and aberrant SRY-box transcription factor 9 (SOX9)-driven bone metabolic reprogramming. FAO: Fatty acid oxidation.*

osteoblasts; the reason for this result may be that gefitinib activated the alternative mechanism of cell proliferation, and its further details and molecular mechanism need to be confirmed in future studies. Consequently, our findings unequivocally demonstrate the capacity of gefitinib to expedite the fracture-healing process, including the resorption phase. Zhu *et al.* confirmed that EGFR strongly inhibited osteoblast differentiation and mineralization (20), while another study reported that in MC3T3-E1 cells, osteogenic differentiation was promoted by EGFR blocking (21). The balance between osteoblasts and osteoclasts ensures the process of fracture healing and repair (2). In line with this, the histological results in our study indicated that gefitinib promoted chondrogenic and osteogenic differentiation in the fracture site, thus contributing to successful fracture repair.

Bone turnover markers, including bone formation resorption markers, can dynamically reflect the whole state of bone metabolism. BALP is currently recognized as a marker of bone formation and of osteoblast phenotype and osteoblast differentiation (22). Furthermore, serum osteogenic markers, PINP, procollagen type I C-terminal propeptide, and CTX can indicate the progress of fracture healing and repair (23-25). Moreover, COL2 and COL10 are used as markers of differentiation of mature chondrocytes (26). In our study, serum markers BALP, osteocalcin, TRAP, and CTX were found to be significantly elevated in the gefitinib-treated group, suggesting that gefitinib promoted cartilage crusts and bony callus formation. The comprehensive analysis of bone turnover markers and serum indicators collectively underscores the capacity of gefitinib to expedite the process of fracture healing and repair.

Fracture healing constitutes a highly intricate process, wherein various phenotypes such as proliferation, invasion, apoptosis, and differentiation of PSCs orchestrate pivotal roles, with chondrogenic differentiation emerging as a central step. Given the constrained local nutritional resources during fracture repair, certain cells may be compelled to engage in alternative metabolic pathways. In

this context, the establishment of 'metabolic symbiosis' emerges as a potential strategy to navigate the challenging milieu of the fracture callus. Specifically, in fracture sites characterized by poor blood supply, PSCs prioritize the initiation of glycolysis due to the scarcity of lipids, thereby curtailing the process of FAO to fulfill their survival requisites amidst environmental pressures (17). In response to this pressure, PSCs undergo metabolic reprogramming, leading to increased chondrocyte differentiation, consequently contributing to delayed fracture healing. Our study revealed that following treatment with LRS, the differentiation of PSCs into chondrocytes was promoted, as evidenced by reduced COL1A1 and COL2A1, alongside a notable increase in SOX9 expression. Furthermore, gefitinib was observed to downregulate the expression of SOX9. These findings suggest that gefitinib modulates chondrocyte differentiation by targeting SOX9.

Moreover, our results further substantiated that gefitinib attenuated glucose uptake, lactate production, and ATP generation in PSCs, thereby diminishing their glycolytic capacity. Importantly, this effect was reversed by the overexpression of *Sox9.* Additionally, the OCR assay corroborated that gefitinib enhances the oxygen consumption level, basal mitochondrial respiration, and maximal mitochondrial capacity of PSCs, thereby augmenting cellular oxidative phosphorylation metabolism. Gefitinib also demonstrated the ability to bolster FAO metabolism, as evidenced by increased FAO-related oxygen consumption and palmitic acid oxidative phosphorylation. Notably, these effects could likewise be reversed by Sox9. Collectively, these results suggest that gefitinib intervenes in the regulation of lipid metabolism and the FAO process through *Sox9* modulation.

Conclusion

Our findings revealed that the administration of gefitinib led to heightened formation and improved quality of bone callus, underscoring its potential to enhance the quality of fracture healing and expedite the recovery of femoral fractures in rats. Molecular mechanism investigations implicated gefitinib in the regulation of lipid metabolism and the FAO process through its interaction with SOX9. Consequently, delving deeper into the role of EGFR regulation in bone healing may yield novel insights into the biology of bone repair and unveil potential therapeutic targets for enhancing bone healing.

Funding

The Authors gratefully acknowledge the support from the National Natural Science Foundation of China (no. 81601902), the China Postdoctoral Science Foundation (no. 2015M572817), the Natural Science Foundation of Hubei Province (no. 2015CFB240), and the Research Fund of Shanghai Municipal Health Commission for Clinical Research in Medical Science (no. 202040084).

Conflicts of Interest

The Authors declare that they have no conflicts of interest.

Authors' Contributions

Ning Xu: Conceptualization, data curation, formal analysis, investigation, methodology, project administration, supervision, validation, visualization, writing – original draft. Gongwu Yuan: Conceptualization, data curation, formal analysis, investigation, methodology, supervision, validation, visualization, writing – review and editing. Wenbo Zeng: Data curation, formal analysis, investigation, methodology, project administration, visualization, writing – original draft. Ximing Liu: Data curation, formal analysis, investigation, methodology, resources, software, supervision, validation, visualization, writing – original draft. Ma Wan: Data curation, formal analysis, investigation, methodology, software, writing – original draft. Suyang Xu: Data curation, investigation, methodology, resources, software, supervision, validation, visualization, writing – review and editing. Yikang Bi: Data curation, formal analysis, investigation, methodology, resources, software, visualization, writing – review and editing. Hai Hu: Data curation, formal analysis, investigation,

methodology, resources, visualization, writing – review and editing. Yafeng Xu: Data curation, formal analysis, funding acquisition, investigation, methodology, project administration, resources, supervision, visualization, writing – review and editing. Shenghui Lan: Conceptualization, data curation, formal analysis, funding acquisition, methodology, project administration, software, supervision, validation, writing – review and editing.

Artificial Intelligence (A.I.) Disclosure

Artificial intelligence tools (ChatGPT by OpenAI) were used solely for language editing purposes. These tools did not participate in the research design, data analysis, or interpretation of results. All scientific content was generated, verified, and approved by the authors.

References

1 Camal Ruggieri IN, Cícero AM, Issa JPM, Feldman S: Bone fracture healing: perspectives according to molecular basis. J Bone Miner Metab 39(3): 311-331, 2021. DOI: 10.1007/s00774-020-01168-0

2 Steppe L, Megafu M, Tschaffon-Müller MEA, Ignatius A, Haffner-Luntzer M: Fracture healing research: Recent insights. Bone Rep 19: 101686, 2023. DOI: 10.1016/j.bonr.2023.101686

3 Dong Y, Wu X, Hao Y, Liu W, Hu X, Zhou J, Li X, Wang B: Epiregulin ameliorates ovariectomy-induced bone loss through orchestrating the differentiation of osteoblasts and osteoclasts. J Bone Miner Res: zjaf017, 2025. DOI: 10.1093/jbmr/zjaf017

4 Yi L, Han N, Li Z, Jiang H, Cao Z: Relaxin-2 promotes osteoblastic differentiation mediated by epidermal growth factor and epidermal growth factor receptor signaling. Biotechnol Appl Biochem 72(1): 260-267, 2025. DOI: 10.1002/bab.2661

5 Wang X, Wang S, Mu H, Yang C, Dong W, Wang X, Wang J: Macrophage-derived amphiregulin promoted the osteogenic differentiation of chondrocytes through EGFR/Yap axis and TGF-β activation. Bone 190: 117275, 2025. DOI: 10.1016/j.bone.2024.117275

6 Shen C, Chen JH, Oh H, Park JH: SOX2 is a positive regulator of osteoclast differentiation. Biochem Biophys Res Commun 526(1): 147-153, 2020. DOI: 10.1016/j.bbrc.2020.03.052

7 Jia Q, Liu L, Yu Y, Wulamu W, Jia L, Liu B, Zheng H, Peng Z, Zhang X, Zhu R: Inhibition of EGFR pathway suppresses M1 macrophage polarization and osteoclastogenesis, mitigating titanium particle-induced bone resorption. J Inflamm Res 17: 9725-9742, 2024. DOI: 10.2147/JIR.S484529

8 Hosomi Y, Morita S, Sugawara S, Kato T, Fukuhara T, Gemma A, Takahashi K, Fujita Y, Harada T, Minato K, Takamura K, Hagiwara K, Kobayashi K, Nukiwa T, Inoue A, North-East Japan Study Group: Gefitinib alone *versus* gefitinib plus chemotherapy for non-small-cell lung cancer with mutated epidermal growth factor receptor: NEJ009 study. J Clin Oncol 38(2): 115-123, 2020. DOI: 10.1200/jco.19.01488

9 Liu G, Xie Y, Su J, Qin H, Wu H, Li K, Yu B, Zhang X: The role of EGFR signaling in age-related osteoporosis in mouse cortical bone. Faseb J 33(10): 11137-11147, 2019. DOI: 10.1096/fj.201900436RR

10 Haseeb A, Kc R, Angelozzi M, de Charleroy C, Rux D, Tower RJ, Yao L, Pellegrino da Silva R, Pacifici M, Qin L, Lefebvre V: SOX9 keeps growth plates and articular cartilage healthy by inhibiting chondrocyte dedifferentiation/osteoblastic redifferentiation. Proc Natl Acad Sci U.S.A. 118(8): e2019152118, 2021. DOI: 10.1073/pnas.2019152118

11 Liang J, Liu Q, Xia L, Lin J, Oyang L, Tan S, Peng Q, Jiang X, Xu X, Wu N, Tang Y, Su M, Luo X, Yang Y, Liao Q, Zhou Y: Rac1 promotes the reprogramming of glucose metabolism and the growth of colon cancer cells through upregulating SOX9. Cancer Sci 114(3): 822-836, 2023. DOI: 10.1111/cas.15652

12 He X, Bougioukli S, Ortega B, Arevalo E, Lieberman JR, McMahon AP: Sox9 positive periosteal cells in fracture repair of the adult mammalian long bone. Bone 103: 12-19, 2017. DOI: 10.1016/j.bone.2017.06.008

13 Shintaku Y, Murakami T, Yanagita T, Kawanabe N, Fukunaga T, Matsuzaki K, Uematsu S, Yoshida Y, Kamioka H, Takano-Yamamoto T, Takada K, Yamashiro T: Sox9 expression during fracture repair. Cells Tissues Organs 194(1): 38-48, 2011. DOI: 10.1159/000322557

14 Zha K, Tan M, Hu Y, Hu W, Zhang S, Zhao Y, Lin Z, Zhang W, Xue H, Mi B, Zhou W, Feng Q, Cao F, Liu G: Regulation of metabolic microenvironment with a nanocomposite hydrogel for improved bone fracture healing. Bioact Mater 37: 424-438, 2024. DOI: 10.1016/j.bioactmat.2024.03.025

15 Lane JM, Sandhu HS: Current approaches to experimental bone grafting. Orthop Clin North Am 18(2): 213-225, 1987.

16 Prodinger PM, Burgkart R, Kreutzer K, Liska F, Pilge H, Schmitt A, Knödler M, Holzapfel BM, Hapfelmeier A, Tischer T, Bissinger O: Does anticoagulant medication alter fracture-healing? A morphological and biomechanical evaluation of the possible effects of rivaroxaban and enoxaparin using a rat closed fracture model. PLoS One 11(7): e0159669, 2016. DOI: 10.1371/journal.pone.0159669

17 van Gastel N, Stegen S, Eelen G, Schoors S, Carlier A, Daniëls VW, Baryawno N, Przybylski D, Depypere M, Stiers PJ, Lambrechts D, Van Looveren R, Torrekens S, Sharda A, Agostinis P, Lambrechts D, Maes F, Swinnen JV, Geris L, Van Oosterwyck H, Thienpont B, Carmeliet P, Scadden DT, Carmeliet G: Lipid availability determines fate of skeletal progenitor cells *via* SOX9. Nature 579(7797): 111-117, 2020. DOI: 10.1038/s41586-020-2050-1

18 Schneider MR, Sibilia M, Erben RG: The EGFR network in bone biology and pathology. Trends Endocrinol Metab 20(10): 517-524, 2009. DOI: 10.1016/j.tem.2009.06.008
19 Giannoudis PV, Einhorn TA, Marsh D: Fracture healing: The diamond concept. Injury 38 Suppl 38: S3-S6, 2007. DOI: 10.1016/s0020-1383(08)70003-2
20 Zhu J, Shimizu E, Zhang X, Partridge NC, Qin L: EGFR signaling suppresses osteoblast differentiation and inhibits expression of master osteoblastic transcription factors Runx2 and Osterix. J Cell Biochem 112(7): 1749-1760, 2011. DOI: 10.1002/jcb.23094
21 Yang M, Pan Y, Zhou Y: miR-96 promotes osteogenic differentiation by suppressing HBEGF–EGFR signaling in osteoblastic cells. FEBS Letters 588(24): 4761-4768, 2014. DOI: 10.1016/j.febslet.2014.11.008
22 Kotobuki N, Hirose M, Funaoka H, Ohgushi H: Enhancement of *in vitro* osteoblastic potential after selective sorting of osteoblasts with high alkaline phosphatase activity from human osteoblast-like cells. Cell Transplant 13(4): 377-384, 2004. DOI: 10.3727/000000004783983756
23 Vasikaran SD, Chubb SP, Ebeling PR, Jenkins N, Jones GR, Kotowicz MA, Morris HA, Schneider HG, Seibel MJ, Ward G: Harmonised Australian reference intervals for serum PINP and CTX in adults. Clin Biochem Rev 35(4): 237-242, 2014.
24 Krege JH, Lane NE, Harris JM, Miller PD: PINP as a biological response marker during teriparatide treatment for osteoporosis. Osteoporos Int 25(9): 2159-2171, 2014. DOI: 10.1007/s00198-014-2646-0
25 Vasikaran SD: Utility of biochemical markers of bone turnover and bone mineral density in management of osteoporosis. Crit Rev Clin Lab Sci 45(2): 221-258, 2008. DOI: 10.1080/10408360801949442
26 Li Y, Liu T, Van Halm-Lutterodt N, Chen J, Su Q, Hai Y: Reprogramming of blood cells into induced pluripotent stem cells as a new cell source for cartilage repair. Stem Cell Res Ther 7: 31, 2016. DOI: 10.1186/s13287-016-0290-7